nature climate change

Article

https://doi.org/10.1038/s41558-024-02008-z

High-resolution modelling identifies the Bering Strait's role in amplified Arctic warming

Received: 13 October 2023

Accepted: 4 April 2024

Published online: 8 May 2024

Check for updates

Gaopeng Xu[1], M. Cameron Rencurrel[1], Ping Chang[1,2] ✉, Xiaoqing Liu[1,3], Gokhan Danabasoglu[4], Stephen G. Yeager[4], Michael Steele[5], Wilbert Weijer[6,7], Yuchen Li[8], Nan Rosenbloom[4], Frederic Castruccio[4] & Qiuying Zhang[1]

The Arctic region has warmed nearly four times faster than the global average since 1979, with far-reaching global implications. However, model projections of Arctic warming rates are uncertain and one key component is the ocean heat transport (OHT) into the Arctic Ocean. Here we use high-resolution historical and future climate simulations to show that the OHT through the Bering Strait exerts a more substantial influence on Arctic warming than previously recognized. The high-resolution ensemble exhibits a 20% larger warming rate for 2006–2100 compared with standard low-resolution model simulations. The enhanced Arctic warming in the high-resolution simulations is primarily attributable to an increased OHT through the narrow and shallow Bering Strait that is nearly four times larger than in the low-resolution simulations. Consequently, the projected rate of Arctic warming by low-resolution climate simulations is likely to be underestimated due to the model resolution being insufficient to capture future changes in Bering Strait OHT.

Arctic warming, characterized by an increase in surface air temperature[1], has wide-reaching consequences that extend far beyond local ecosystems. The melting of sea ice and glaciers and the thawing of permafrost in the Arctic are causing substantial transformations in the environment[2–6]. Moreover, recent studies have revealed a potential connection between Arctic warming and extreme weather events in the mid-latitudes of the Northern Hemisphere[7–14]. Given these findings, it is imperative to advance our understanding of future Arctic warming. This improved understanding is vital for effectively adapting to the anticipated impacts and developing appropriate mitigation strategies for the future.

In addition to temperature feedbacks[15,16], research findings consistently affirm the widely accepted notion that Arctic warming is heightened by the reduction in sea ice due to the ice–albedo feedback[17–23]. Within this mechanism, the diminishing sea-ice cover results in greater absorption of solar radiation by the ocean, thereby intensifying atmospheric warming in the Arctic and subsequently driving further sea-ice retreat. Observational and modelling studies indicate a notable relationship between the retreat of sea ice in the Barents and Greenland Seas and the increase in northward ocean heat transport (OHT) through the Barents Sea Opening and Fram Strait[24–29]. Over the period 1997–2007, the OHT through the Barents Sea Opening (50–70 TW) and Fram Strait (~36 ± 6 TW) is stronger than the northward OHT through the Bering Strait (~10–20 TW)[30], resulting in the Atlantic OHT receiving more attention in Arctic warming studies. Nevertheless,

[1]Department of Oceanography, Texas A&M University, College Station, TX, USA. [2]Department of Atmospheric Sciences, Texas A&M University, College Station, TX, USA. [3]Department of Earth, Atmospheric and Planetary Sciences, Purdue University, West Lafayette, IN, USA. [4]National Science Foundation National Center for Atmospheric Research, Boulder, CO, USA. [5]Polar Science Center/Applied Physics Laboratory, University of Washington, Seattle, WA, USA. [6]Los Alamos National Laboratory, Los Alamos, NM, USA. [7]International Arctic Research Center, University of Alaska Fairbanks, Fairbanks, AK, USA. [8]Stanford University, Stanford, CA, USA. ✉e-mail: ping@tamu.edu

recent research has shed light on the crucial role of Pacific OHT through the Bering Strait in driving sea-ice melt. Specifically, the increased OHT through the Bering Strait shows a strong connection with the retreat of sea ice in the Chukchi Sea[31–33], a region that experiences substantial ice loss during the summer[34]. Interestingly, for the same amount of total Arctic OHT, which includes Barents Sea Opening, Bering Strait, Fram Strait and Davis Strait, the reduction in Arctic sea-ice area and volume is more pronounced when there is an increase in sea surface temperature (SST) on the Pacific side compared with an increase on the Atlantic side[35]. These recent findings underscore the importance of considering both the Atlantic and Pacific OHT pathways to comprehensively understand and project changes in Arctic sea ice[36,37].

The Bering Strait is relatively narrow, spanning approximately 85 km, and relatively shallow with an average depth of around 50 m. In many IPCC-class models with ocean resolutions of ~1°, the Bering Strait geometry and ocean hydrography and circulation are not properly represented, resulting in a weaker-than-observed OHT[29,38]. Enhanced ocean resolution can help to better represent ocean pathways in the openings into the Arctic, such as the Barents Sea[39]. This could potentially influence the simulated OHT into the Arctic[40–44]. While there is no consensus on a systematic increase in OHT to the Arctic with model resolution increases among Coupled Model Intercomparison Project (CMIP) models[39,45], a recent modelling study suggested that increasing ocean resolution from 1° to 0.1° or 0.25° leads to an increased Bering Strait OHT[44]. This suggests that the impact of OHT through the Bering Strait on sea-ice loss and Arctic warming might be underestimated by most models that have a nominal horizontal resolution of ~1°.

In this study we assess the importance of accurately simulating OHT through the Bering Strait to better understand Arctic warming. By analysing multi-century high-resolution and low-resolution climate simulations (HR and LR) using the Community Earth System Model[46–49] (CESM; Methods), we explore the relationships between Bering Strait OHT, sea-ice loss and Arctic warming. We begin our analyses by first validating HR and LR through comparison with available observations, and then explore the influence of Bering Strait OHT on Arctic warming. All results presented here are based on the mean of three ensemble members in HR and five ensemble members in LR.

Model–observation comparison

We compared satellite-observed[50,51] and model-simulated SST during August–September–October (ASO) in the Bering Strait region (Fig. 1a–d). ASO is a critical period for monitoring and understanding the state of Arctic sea-ice cover and its temporal changes, as it corresponds to the time when Arctic sea ice reaches its minimum extent following the summer melting season. The observations reveal that the warmest SST in this region is located along the west coast of Alaska, while the coldest SSTs are observed along eastern Siberia with a distinct SST gradient across the Bering Strait (Fig. 1a). HR generally captured this pattern well (Fig. 1b), although the values of the warmest SST in the east and the coldest SST in the west show some differences from the observations. In contrast, LR failed to capture many detailed features of the observed SST, with a weaker SST gradient across the Bering Strait (Fig. 1c). The multi-model ensemble mean (MMEM) of CMIP Phase 5 (CMIP5) simulations, forced by identical external climate forcing to LR at a comparable resolution, exhibited a pattern akin to that of LR (Fig. 1d), both revealing a substantial cold SST bias.

To compare simulated OHT through the Bering Strait to observations, we used OHT estimates inferred from two moorings near the Bering Strait[32] as the observational baseline. The mooring-based OHT exhibited a distinct seasonal cycle, reaching its peak around August with a magnitude of 42 ± 5 TW[32] (Fig. 1e). Model-derived OHT in HR reasonably captured this seasonal variation, albeit with a peak magnitude overestimated by 30%. In contrast, model-derived OHT in LR underestimated the mooring-based peak by 34% (Fig. 1e). When we determined OHT in HR and LR using the same inferred calculation method used for the mooring-based estimates (Methods), the estimated peak in LR was nearly four times smaller than the observations. However, the OHT estimated by the inferred calculation method in HR closely replicated the model-derived OHT (Extended Data Fig. 1a). The stronger OHT in HR is attributed not only to the temperature (Fig. 1a–d), but also to the northward volume transport difference between HR and LR (Fig. 1f). Compared with mooring-based estimates, HR overestimated the peak magnitude of the northward volume transport by 25%, while LR underestimated it by 63%. The mooring-based Bering Strait OHT also showed notable interannual variability and an increasing trend[32] (Fig. 1g) that was only captured by HR. The standard deviation of the annual mean OHT from 2000–2021 in HR, ranging from 3.8 TW to 4.8 TW across ensemble members, was comparable to the mooring-based estimate of 3.0 TW (Extended Data Fig. 2a). The OHT trend in HR was 2.1 TW per decade (dec), whereas the mooring-based trend stands at 1.6 TW dec^{-1} over 2010–2021. However, it is important to note that the trends in the observations and HR did not achieve statistical significance at the 95% confidence level due to the pronounced interannual variability and the short duration of the record. In contrast, LR exhibited a much weaker variability in simulated OHT (Extended Data Fig. 2a) with no discernible trend (Fig. 1g).

The high level of realism achieved by HR is further demonstrated by comparing observed and simulated sea-ice-area changes in the vicinity of the Bering Strait (Fig. 1h and Extended Data Fig. 3). The observed sea-ice area had a declining trend of 0.025 million km^2 dec^{-1} from 1979 to 2022 at the 95% confidence level. In comparison, HR exhibited a less pronounced declining trend of 0.015 million km^2 dec^{-1} during the same period, while LR showed a declining trend of 0.010 million km^2 dec^{-1}, approximately 50% weaker than that of HR. Therefore, although both HR and LR underestimated the declining trend in the observations, HR showed a noticeable improvement. It is also important to note that the trends in HR and LR were based on ensemble means, which may contribute to the weaker model trends, as internal variability could contribute to the stronger observed trend[52,53]. After removing the linear trend, the annual mean sea-ice area showed a covariation with the Bering Strait OHT, characterized by a correlation coefficient of −0.86. This relationship was more accurately depicted by HR than by LR (Extended Data Fig. 2b).

In conclusion, the above analysis highlights that HR simulations provide a considerably more accurate representation of the climatology and variability of Bering Strait OHT, SST and sea-ice area. This improved fidelity enhances the credibility of HR simulations in capturing future changes in Bering Strait OHT and its consequential impact on Arctic warming.

Projected Arctic warming

In the high-emissions scenario (RCP8.5), the Arctic surface air temperature is projected to undergo warming at a rate of 1.28 °C dec^{-1} in HR over the period 2006–2100 (Fig. 2a). This warming rate was approximately 20% higher than the rate projected by LR. Moreover, the change in surface air temperature in HR surpassed the CMIP5 MMEM, which indicates a warming trend of 0.97 ± 0.17 °C dec^{-1}, by more than one ensemble standard deviation. This underscores the large disparity between Arctic warming projections in HR and LR.

The strongest Arctic warming in HR was located near the Canadian Arctic Archipelago and Greenland (Fig. 2b), sharing a similar spatial pattern with the historical sea-ice concentration[46], which underscores the importance of sea-ice melting in the future. The spatial pattern of warming rates was generally similar between HR and LR, as evident from Fig. 2b and Extended Data Fig. 4. However, HR exhibited a more pronounced warming rate in most Arctic regions (the central Arctic, eastern Arctic, Canadian Archipelago, Beaufort Sea, Chukchi Sea and so on), while showing a smaller rate of warming over the Barents Sea and Greenland Sea (Fig. 2c). This result clearly indicates that the amplified Arctic warming in HR is primarily attributed to the warming difference between HR and LR across the Pacific sector (66° N–90° N, 120° E–240° E; cyan outline in Fig. 2c).

https://doi.org/10.1038/s41558-024-02008-z

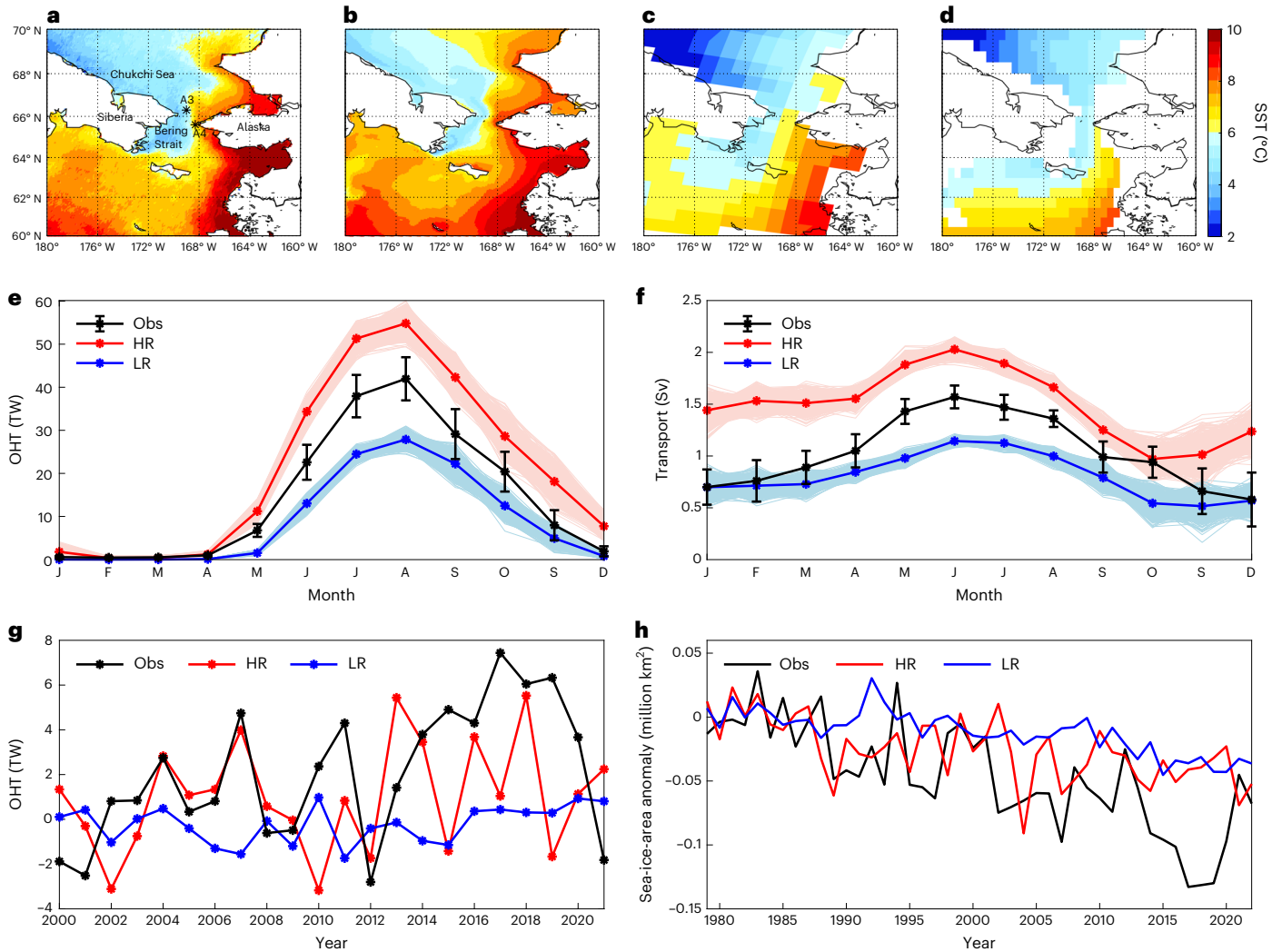

Fig. 1 | Model–observation comparison near the Bering Strait. a–**d**, SST in ASO from observations (**a**, MODIS/Aqua level 3 Mapped Thermal and Mid-IR SST[50,51]), HR (**b**), LR (**c**) and CMIP5 MMEM simulations (**d**). Sites A3 and A4 in **a** are used to construct OHT using the inferred calculation method (Methods). **e**, Seasonal cycle of model-derived OHT through the Bering Strait from the mooring-based estimates[32] (observations, obs), HR and LR. Shaded regions represent the model uncertainty determined using a bootstrap sampling method (Methods). **f**, Similar to **e** but for northward volume transport. **g**, Similar to **e** but for annual mean OHT changes relative to the 2000–2004 mean. SST and OHT climatologies in **a**–**f** are based on averages over the period 2003–2015. Error bars in **e** and **f** are the 95% limit of a one-sided Student's *t*-test with the degree of freedom set to 13 (ref. 32). **h**, Annual mean sea-ice-area anomalies relative to the 1979–1988 mean. The region used to construct the time series of sea-ice area is shown by the green shading in Extended Data Fig. 3. The NOAA/NSIDC Climate Data Record of Passive Microwave Monthly Sea Ice Concentration[63] is used to construct sea-ice area. Note that the analysis utilizes different time periods for various variables, aligning with variations in the record lengths of corresponding observations. The model results correspond to the same respective observational time periods.

Given that the retreat of sea ice in the Pacific sector of the Arctic is significantly correlated with OHT through the Bering Strait[29], which is also seen in Extended Data Fig. 3, we next examined the relationship between Bering Strait OHT and surface warming. Here the OHT was computed using model-derived output, not using the inferred calculation. The increase in Bering Strait OHT was considerably more rapid in HR compared with LR, particularly after 2030 (Fig. 3a). This disparity between HR and LR OHT projections continued to amplify with higher concentrations of CO_2. From 2006 to 2100, OHT increased at a rate of 0.31 TW yr^{-1} (0.09 TW yr^{-1}) in HR (LR). By decomposing the changes in OHT into components induced by temperature changes ($v\Delta T$) and velocity changes ($T\Delta v$) (Methods), we found that the warming of the Bering Strait throughflow waters predominantly drives changes in OHT (Extended Data Fig. 5), consistent with findings from other modelling studies[29,54]. The trend of OHT from LR aligned with those of the CMIP5 MMEM. Similarly, in line with surface air temperature, OHT in HR surpassed one ensemble standard deviation above the MMEM.

A clear correlation at the 95% confidence level between changes in simulated Bering Strait OHT and future Arctic warming was detected in CMIP5 models (Fig. 3b). Models that exhibit larger increases in OHT are associated with more pronounced Arctic warming. Specifically, a 1 TW increase in OHT approximately corresponds to a 0.15 °C increase in surface air temperature. Remarkably, both HR and LR closely adhered to this statistical relationship, with the HR values residing at the far end of the ensemble spread. It clearly highlights a shared sensitivity among different climate models regarding future Arctic warming and changes in Bering Strait OHT.

It is important to emphasize that this sensitivity of Arctic warming to Bering Strait OHT is only found within the Pacific sector (Extended Data Fig. 6a). No significant relationship with surface air temperature was found in the Atlantic sector (Extended Data Fig. 6b). This implies that the influence of Bering Strait OHT on surface air temperature is limited to the Pacific sector. Within the Pacific sector, a linear regression analysis revealed that a 1 TW increase in OHT corresponded to warming

https://doi.org/10.1038/s41558-024-02008-z

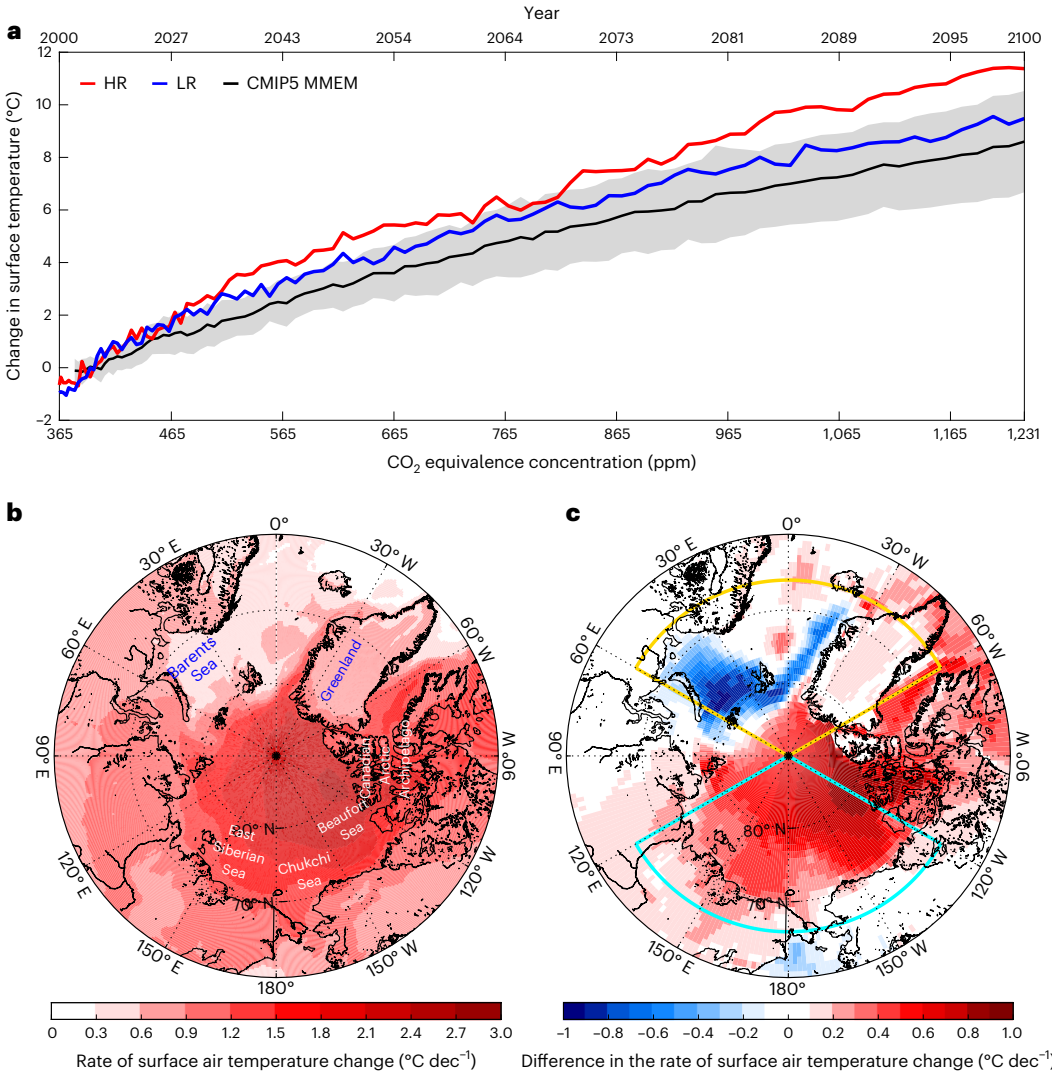

Fig. 2 | Projected Arctic warming. a, Annual mean Arctic-averaged surface air temperature changes relative to the 2006–2015 mean in HR, LR and CMIP5 MMEM simulations under RCP8.5. The grey shading shows the range of one ensemble standard deviation above and below the MMEM. The Arctic region is defined as the area north of 66° N. CO_2 equivalence concentration is the concentration of various greenhouse gases in terms of the amount of CO_2 that would produce the same global warming effect. **b**, The rate of surface air temperature changes in HR over the period 2006–2100. **c**, The difference in the rate of surface air temperature changes between HR and LR (HR − LR). The cyan (yellow) outline is the Pacific (Atlantic) sector of the Arctic 66° N–90° N, 120° E–240° E (66° N–90° N, 60° W–60° E).

of roughly 0.22 °C, which is higher than the Arctic-averaged warming of 0.15 °C by nearly 47%. Numerous studies have correlated the sea-ice loss in the Chukchi Sea with the increase in OHT based on both observations[31,33,55,56] and numerical models[35,38,54,57]. We hypothesize that sea ice serves as a physical link between Bering Strait OHT and Arctic warming. With an increase in OHT through the Bering Strait, more sea ice in the Pacific sector of the Arctic Ocean is prompted to melt. This, in turn, can result in an increase in latent and sensible heat release into the atmosphere, initiating positive feedback loops between surface heat flux and sea-ice changes, including the ice–albedo feedback. These feedback mechanisms contribute to accelerated Arctic warming. Consequently, changes in Bering Strait OHT play a pivotal role in shaping future Arctic warming, and it is evident that accurately modelling Bering Strait OHT is indispensable to generate reliable projections of Arctic warming.

Sea ice linking Bering Strait OHT and Arctic warming

The large differences in Bering Strait OHT changes among HR, LR and CMIP5 models were primarily seen during the boreal winter and spring seasons (Extended Data Fig. 7). These differences suggest that sea-ice changes in the region may serve as a key link between increased OHT and Arctic warming. This is because there is sea ice in the Bering Sea and Chukchi Sea in winter and spring, while there is not in summer. To understand the implications of the differences in future OHT changes for sea ice within the Pacific sector of the Arctic between HR and LR, we compared sea-ice changes during the boreal spring season (March–April–May, MAM) (Fig. 4). The Arctic sea-ice concentration reaches its maximum in March[46], coinciding with the end of polar night, and the MAM period marks the transition from sea-ice peak conditions to melting. Starting from 2030, HR revealed a gradual increase in spring sea-ice loss extending from the Bering Strait towards the central Arctic, with an acceleration towards the end of the century (Fig. 4a–d and Extended Data Fig. 8a–d). In contrast, no substantial sea-ice loss was evident in LR north of the Bering Strait during this season (Fig. 4e–h). Both HR and LR showed an increase in turbulent surface heat flux from the ocean to the atmosphere, as well as an increase in the net shortwave surface heat flux (SW) into the ocean, due to the expansion of sea-ice-free areas (Fig. 4i–p), but in LR the changes were only observed to the south of the

https://doi.org/10.1038/s41558-024-02008-z

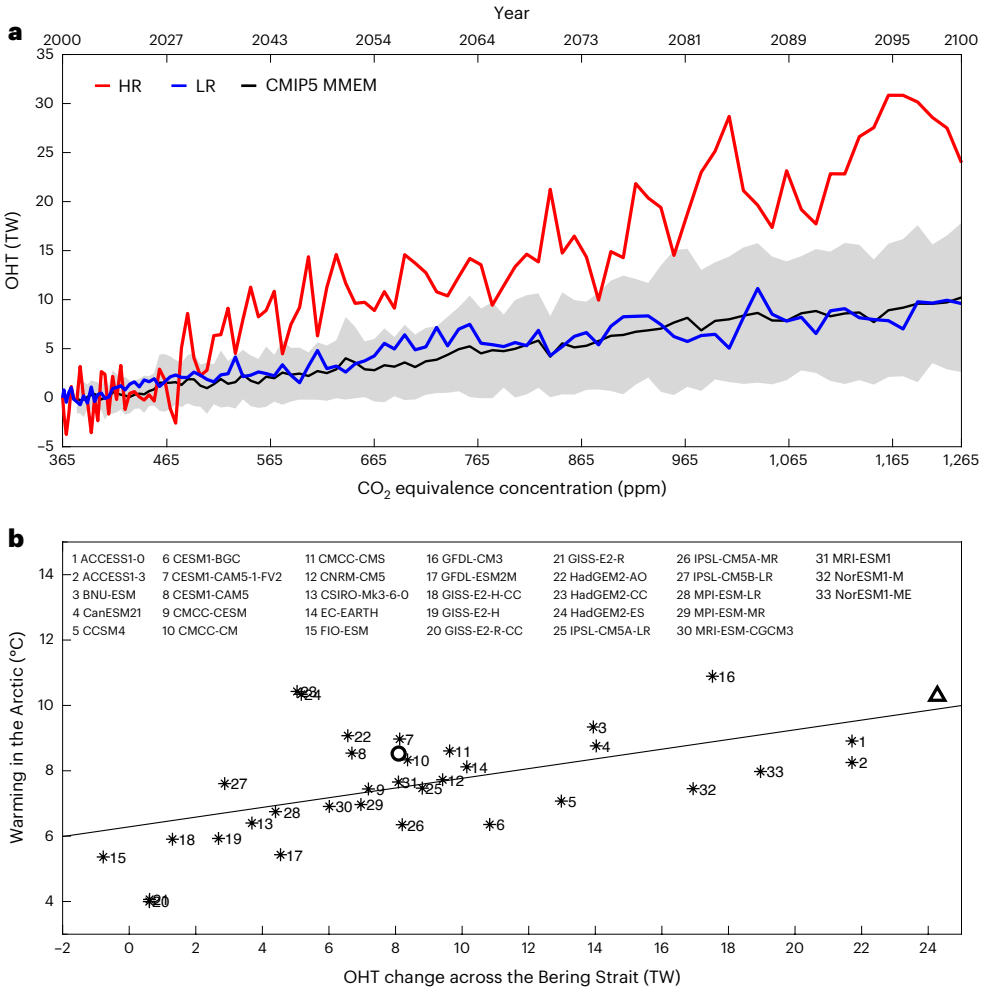

Fig. 3 | Relationship between projected changes in Bering Strait OHT and Arctic warming. a, OHT changes relative to the 2006–2015 mean as a function of CO_2 concentration increase (bottom *x* axis) and time (top *x* axis) in HR, LR and CMIP5 MMEM simulations under RCP8.5. The grey shading represents the range of one ensemble standard deviation above and below the MMEM. **b**, Scatter plot of changes in Bering Strait OHT and Arctic-averaged surface air temperature in HR (triangle), LR (circle) and CMIP5 models (stars, 1–33). See Supplementary Table 1 for more details of the CMIP5 models. The changes in **b** are defined as the difference between the 2081–2100 mean and the 2006–2015 mean. OHT in CMIP5 models is calculated using monthly mean temperature and velocity. The black solid line in **b** is linear regression based on CMIP5 models that passes the 95% significance test with a slope of 0.15 °C TW^{-1}.

Bering Strait. From the 2070s to the end of the century, HR exhibited accelerated sea-ice loss in the central Arctic with a strong SW response (Fig. 4d,l and Extended Data Fig. 8d). In comparison, those changes in LR remained more limited and weaker (Fig. 4h,p). The notable disparities in sea-ice loss and SW response between HR and LR during the boreal spring have substantial implications not only for sea-ice melting in the following summer, but also for sea-ice formation in the subsequent winter.

Compared with the spring season, the SW response is absent in the Arctic during winter due to the lack of solar radiation, but the warmer ocean conditions driven by the stronger SW response from previous seasons can impede the growth of sea ice during winter. The declining patterns of basal sea-ice growth closely corresponded to the warming of ocean temperatures within the upper 50 m (Extended Data Fig. 9a–h). Note that by the end of the century, the winter sea-ice edge will recede substantially northwards of the Bering Strait (Extended Data Fig. 8l). This shift in the sea-ice edge position is the reason behind the notably warm upper ocean and surface air temperatures. A warmer ocean can also lead to thinner and more vulnerable ice cover, making it more susceptible to break-up and melting during winter storms or when exposed to warmer air temperatures[58,59]. When combined with the stronger OHT through the Bering Strait during the boreal winter in HR, the result was much less sea-ice formation compared with LR. Consequently, there were increased turbulent heat fluxes from the ocean to the atmosphere (Extended Data Fig. 9i–p). These findings suggest that the differences in Arctic warming rates between HR and LR were probably attributable to Bering Strait OHT-induced sea-ice loss, which directly influences the air–sea heat exchange. It is worth noting that HR exhibited a more pronounced negative sea-ice bias over the Arctic than LR[46]. However, a detailed analysis of sea-ice bias indicated that the majority of the negative sea-ice bias in HR was concentrated in the Atlantic sector of the Arctic, and the bias over the Pacific sector was less severe in HR than in LR. Consequently, it is unlikely that the sea-ice bias substantially impacted the findings of this study.

Conclusions

Several studies[29,32,60,61] have documented the anomalous advection of warm Pacific Water into the Arctic through the Bering Strait, referred to as Pacification. Under the RCP8.5 emissions scenario, our study reveals that HR projects a more rapid increase in Bering Strait OHT than LR and other CMIP5 model simulations. The intensified Bering Strait OHT in HR results in accelerated sea-ice loss in the Pacific sector of the Arctic, strengthening the increase in SW absorption in the region. Consequently, more heat is released from the ocean to the atmosphere

https://doi.org/10.1038/s41558-024-02008-z

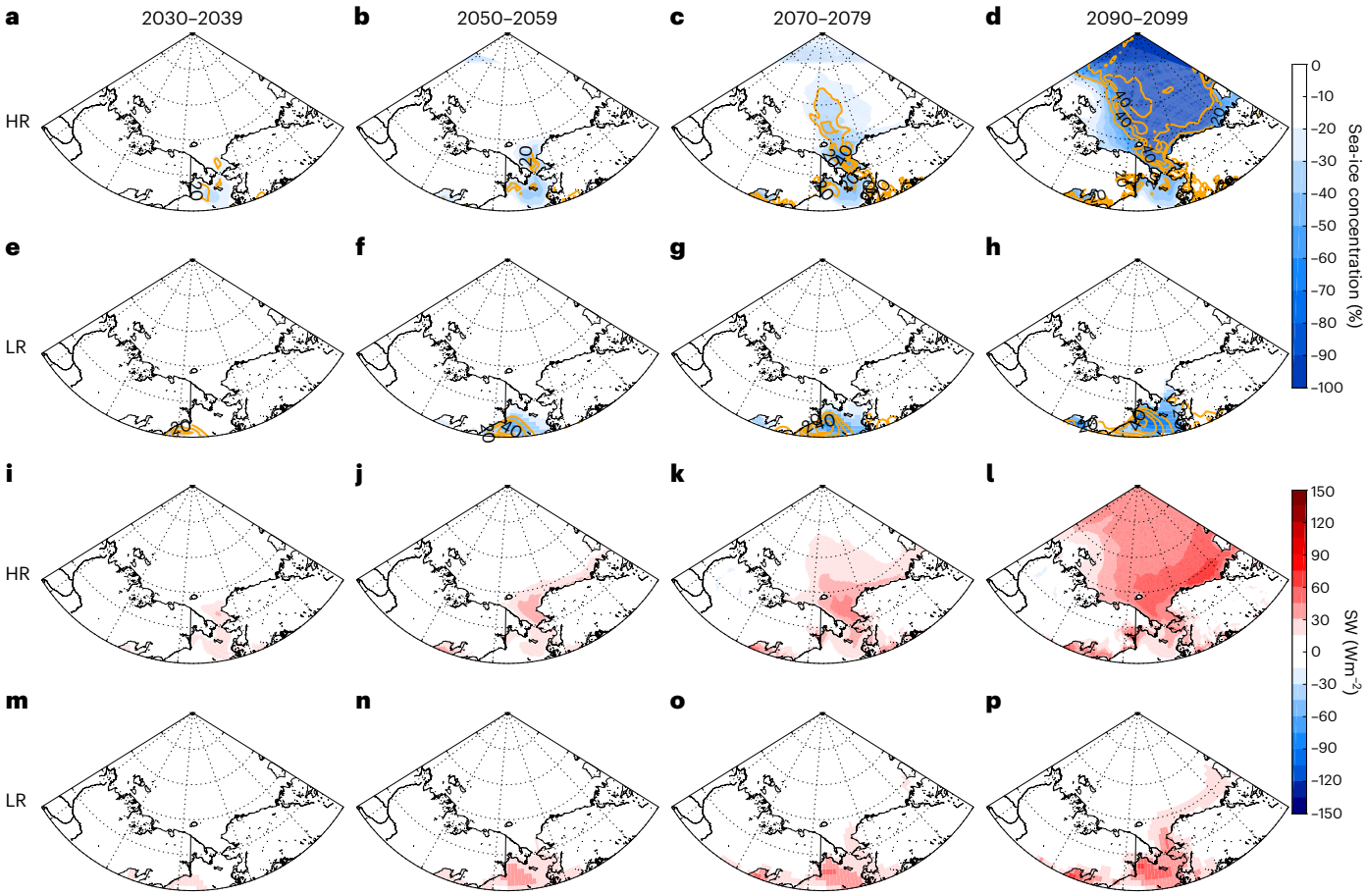

Fig. 4 | Future changes in sea-ice concentration and surface heat fluxes. **a**–**d**, Changes in sea-ice concentration during boreal spring (MAM) in HR (colour shading) averaged over the periods shown at the top relative to the mean over 2006–2015. The contours represent turbulent heat flux during MAM at 10 W m^{-2} intervals with 20 and 40 W m^{-2} labelled. Positive turbulent heat flux is upwards (from the ocean to the atmosphere). **e**–**h**, Same as **a**–**d** but for LR. **i**–**l**, Changes in SW during MAM in HR in the same respective periods as **a**–**d**. **m**–**p**, Same as **i**–**l** but for LR. Positive shortwave surface heat flux is downwards (from the atmosphere to the ocean).

in HR than in LR. The larger heat release in HR would lead to greater Arctic warming in HR. These findings indicate that CMIP-class models are probably underestimating the influence of the Bering Strait OHT on Arctic warming. Despite the small spatial extent of the Bering Strait within the global ocean, the corresponding OHT can have a substantial upscaling impact on the larger climate system. It is therefore crucial to recognize the need to improve the representation of Bering Strait OHT and its impacts in future model developments.

By increasing the ocean resolution to 0.1° and atmosphere resolution to 0.25° in CESM, we observed that Bering Strait OHT, volume transport, SST and sea-ice changes in the Pacific sector of the Arctic aligned more closely with observations. A recent study highlights that Bering Strait volume transport emerges as a pivotal factor influencing the strength of the coupling between Bering Strait OHT and sea-ice changes[62]. These improvements boost confidence in projecting the effects of Pacification using HR. However, the Pacification mechanism revealed by HR would benefit from further validation through other high-resolution long-term climate simulations and longer-term ocean observations. Nevertheless, the long record of surface air temperature observations does indicate that the Pacific sector of the Arctic has been warming at a faster rate than the entire Arctic region since the mid-1970s. Conversely, the Atlantic sector shows a less pronounced warming trend in comparison with the broader Arctic region (Extended Data Fig. 10). While these observations align with the findings from HR, more observations are required to conclusively confirm the prominent role of the Pacification mechanism in future Arctic warming. Although the results in this study suggest a potential driving role of Bering Strait OHT in future Arctic warming, further investigations are required to validate this claim. Interactions among Bering Strait OHT, sea-ice loss and Arctic warming are highly complex. To fully determine the role of Bering Strait OHT and causality among these interactive processes, future process-level sensitivity experiments are necessary. Future high-resolution model intercomparison studies are also critical to fully elucidate the role of Bering Strait OHT in Arctic warming.

Online content

Any methods, additional references, Nature Portfolio reporting summaries, source data, extended data, supplementary information, acknowledgements, peer review information; details of author contributions and competing interests; and statements of data and code availability are available at https://doi.org/10.1038/s41558-024-02008-z.

References

1. Rantanen, M. et al. The Arctic has warmed nearly four times faster than the globe since 1979. *Commun. Earth Environ.* **3**, 168 (2022); https://doi.org/10.1038/s43247-022-00498-3
2. Walter Anthony, K. M., Anthony, P., Grosse, G. & Chanton, J. Geologic methane seeps along boundaries of Arctic permafrost thaw and melting glaciers. *Nat. Geosci.* **5**, 419–426 (2012).
3. Grémillet, D. et al. Arctic warming: nonlinear impacts of sea-ice and glacier melt on seabird foraging. *Glob. Change Biol.* **21**, 1116–1123 (2015).

4. Hjort, J. et al. Degrading permafrost puts Arctic infrastructure at risk by mid-century. *Nat. Commun.* **9**, 5147 (2018); https://doi.org/10.1038/s41467-018-07557-4
5. Miner, K. R. et al. Emergent biogeochemical risks from Arctic permafrost degradation. *Nat. Clim. Change* **11**, 809–819 (2021).
6. Fox-Kemper, B. et al. in *Climate Change 2021: The Physical Science Basis* (eds Masson-Delmotte, V. et al.) 1211–1361 (IPCC, Cambridge Univ. Press, 2021).
7. Wallace, J. M., Held, I. M., Thompson, D. W., Trenberth, K. E. & Walsh, J. E. Global warming and winter weather. *Science* **343**, 729–730 (2014).
8. Cohen, J. et al. Recent Arctic amplification and extreme mid-latitude weather. *Nat. Geosci.* **7**, 627–637 (2014).
9. Francis, J. A. & Vavrus, S. J. Evidence for a wavier jet stream in response to rapid Arctic warming. *Environ. Res. Lett.* **10**, 014005 (2015).
10. Kug, J.-S. et al. Two distinct influences of Arctic warming on cold winters over North America and East Asia. *Nat. Geosci.* **8**, 759–762 (2015).
11. Overland, J. E. et al. Nonlinear response of mid-latitude weather to the changing Arctic. *Nat. Clim. Change* **6**, 992–999 (2016).
12. Zhang, R., Sun, C., Zhu, J., Zhang, R. & Li, W. Increased European heat waves in recent decades in response to shrinking Arctic sea ice and Eurasian snow cover. *npj Clim. Atmos. Sci.* **3**, 7 (2020); https://doi.org/10.1038/s41612-020-0110-8
13. Tang, Q., Zhang, X. & Francis, J. A. Extreme summer weather in northern mid-latitudes linked to a vanishing cryosphere. *Nat. Clim. Change* **4**, 45–50 (2014).
14. Cohen, J. et al. Divergent consensuses on Arctic amplification influence on midlatitude severe winter weather. *Nat. Clim. Change* **10**, 20–29 (2020).
15. Pithan, F. & Mauritsen, T. Arctic amplification dominated by temperature feedbacks in contemporary climate models. *Nat. Geosci.* **7**, 181–184 (2014).
16. Goosse, H. et al. Quantifying climate feedbacks in polar regions. *Nat. Commun.* **9**, 1919 (2018); https://doi.org/10.1038/s41467-018-04173-0
17. Johannessen, O. M. et al. Arctic climate change: observed and modelled temperature and sea-ice variability. *Tellus A* **56**, 328–341 (2004).
18. Serreze, M., Barrett, A., Stroeve, J., Kindig, D. & Holland, M. The emergence of surface-based Arctic amplification. *Cryosphere* **3**, 11–19 (2009).
19. Comiso, J. C., Parkinson, C. L., Gersten, R. & Stock, L. Accelerated decline in the Arctic sea ice cover. *Geophys. Res. Lett.* **35**, L01703 (2008); https://doi.org/10.1029/2007GL031972
20. Screen, J. A. & Simmonds, I. The central role of diminishing sea ice in recent Arctic temperature amplification. *Nature* **464**, 1334–1337 (2010).
21. Polyak, L. et al. History of sea ice in the Arctic. *Quat. Sci. Rev.* **29**, 1757–1778 (2010).
22. Lind, S., Ingvaldsen, R. B. & Furevik, T. Arctic warming hotspot in the northern Barents Sea linked to declining sea-ice import. *Nat. Clim. Change* **8**, 634–639 (2018).
23. Dai, A., Luo, D., Song, M. & Liu, J. Arctic amplification is caused by sea-ice loss under increasing CO_2. *Nat. Commun.* **10**, 121 (2019); https://doi.org/10.1038/s41467-018-07954-9
24. Smedsrud, L. H., Ingvaldsen, R., Nilsen, J. & Skagseth, Ø. Heat in the Barents Sea: transport, storage, and surface fluxes. *Ocean Sci.* **6**, 219–234 (2010).
25. Årthun, M., Eldevik, T., Smedsrud, L., Skagseth, Ø. & Ingvaldsen, R. Quantifying the influence of Atlantic heat on Barents Sea ice variability and retreat. *J. Clim.* **25**, 4736–4743 (2012).
26. van der Linden, E. C., Le Bars, D., Bintanja, R. & Hazeleger, W. Oceanic heat transport into the Arctic under high and low CO_2 forcing. *Clim. Dynam.* **53**, 4763–4780 (2019).
27. Li, D., Zhang, R. & Knutson, T. R. On the discrepancy between observed and CMIP5 multi-model simulated Barents Sea winter sea ice decline. *Nat. Commun.* **8**, 14991 (2017); https://doi.org/10.1038/ncomms14991
28. Årthun, M., Eldevik, T. & Smedsrud, L. H. The role of Atlantic heat transport in future Arctic winter sea ice loss. *J. Clim.* **32**, 3327–3341 (2019).
29. Dörr, J., Årthun, M., Eldevik, T. & Madonna, E. Mechanisms of regional winter sea-ice variability in a warming Arctic. *J. Clim.* **34**, 8635–8653 (2021).
30. Beszczynska-Möller, A., Woodgate, R. A., Lee, C., Melling, H. & Karcher, M. A synthesis of exchanges through the main oceanic gateways to the Arctic Ocean. *Oceanography* **24**, 82–99 (2011).
31. Woodgate, R. A., Weingartner, T. & Lindsay, R. The 2007 Bering Strait oceanic heat flux and anomalous Arctic sea-ice retreat. *Geophys. Res. Lett.* **37**, L01602 (2010); https://doi.org/10.1029/2009GL041621
32. Woodgate, R. A. Increases in the Pacific inflow to the Arctic from 1990 to 2015, and insights into seasonal trends and driving mechanisms from year-round Bering Strait mooring data. *Prog. Oceanogr.* **160**, 124–154 (2018).
33. Serreze, M. C., Barrett, A. P., Crawford, A. D. & Woodgate, R. A. Monthly variability in Bering Strait oceanic volume and heat transports, links to atmospheric circulation and ocean temperature, and implications for sea ice conditions. *J. Geophys. Res. Oceans* **124**, 9317–9337 (2019).
34. Stroeve, J. & Notz, D. Changing state of Arctic sea ice across all seasons. *Environ. Res. Lett.* **13**, 103001 (2018).
35. Docquier, D., Koenigk, T., Fuentes-Franco, R., Karami, M. P. & Ruprich-Robert, Y. Impact of ocean heat transport on the Arctic sea-ice decline: a model study with EC-Earth3. *Clim. Dynam.* **56**, 1407–1432 (2021).
36. Mahlstein, I. & Knutti, R. Ocean heat transport as a cause for model uncertainty in projected Arctic warming. *J. Clim.* **24**, 1451–1460 (2011).
37. Carmack, E. et al. Toward quantifying the increasing role of oceanic heat in sea ice loss in the new Arctic. *Bull. Am. Meteorol. Soc.* **96**, 2079–2105 (2015).
38. Auclair, G. & Tremblay, L. B. The role of ocean heat transport in rapid sea ice declines in the Community Earth System Model Large Ensemble. *J. Geophys. Res. Oceans* **123**, 8941–8957 (2018).
39. Docquier, D., Fuentes-Franco, R., Koenigk, T. & Fichefet, T. Sea ice–ocean interactions in the Barents Sea modeled at different resolutions. *Front. Earth Sci.* **8**, 172 (2020).
40. Roberts, C. D. et al. Climate model configurations of the ECMWF Integrated Forecasting System (ECMWF-IFS cycle 43r1) for HighResMIP. *Geosci. Model Dev.* **11**, 3681–3712 (2018).
41. Clement Kinney, J. et al. On the flow through the Bering Strait: A synthesis of model results with observations, in *The Pacific Arctic Region. Ecosystem Status and Trends in a Rapidly Changing Environment* (eds Grebmeier J. M. & Maslowski W.) 167–198 (Springer, 2014).
42. Roberts, M. J. et al. Description of the resolution hierarchy of the global coupled HadGEM3-GC3.1 model as used in CMIP6 HighResMIP experiments. *Geosci. Model Dev.* **12**, 4999–5028 (2019).
43. Griffies, S. M. et al. Impacts on ocean heat from transient mesoscale eddies in a hierarchy of climate models. *J. Clim.* **28**, 952–977 (2015).
44. Decuypère, M., Tremblay, L. B. & Dufour, C. O. Impact of ocean heat transport on Arctic sea ice variability in the GFDL CM2-O model suite. *J. Geophys. Res. Oceans* **127**, e2021JC017762 (2022).

45. Madonna, E. & Sandø, A. B. Understanding differences in North Atlantic poleward ocean heat transport and its variability in global climate models. *Geophys. Res. Lett.* **49**, e2021GL096683 (2022).
46. Chang, P. et al. An unprecedented set of high-resolution earth system simulations for understanding multiscale interactions in climate variability and change. *J. Adv. Model. Earth Syst.* **12**, e2020MS002298 (2020).
47. Chang, P. et al. Uncertain future of sustainable fisheries environment in eastern boundary upwelling zones under climate change. *Commun. Earth Environ.* **4**, 19 (2023).
48. Small, R. J. et al. A new synoptic scale resolving global climate simulation using the Community Earth System Model. *J. Adv. Model. Earth Syst.* **6**, 1065–1094 (2014).
49. Meehl, G. A. et al. Effects of model resolution, physics, and coupling on Southern Hemisphere storm tracks in CESM1.3. *Geophys. Res. Lett.* **46**, 12408–12416 (2019).
50. Walton, C., Pichel, W., Sapper, J. & May, D. The development and operational application of nonlinear algorithms for the measurement of sea surface temperatures with the NOAA polar-orbiting environmental satellites. *J. Geophys. Res. Oceans* **103**, 27999–28012 (1998).
51. Brown, O. B. et al. MODIS infrared sea surface temperature algorithm algorithm theoretical basis document version 2.0. (Univ. of Miami, 1999); https://oceancolor.gsfc.nasa.gov/docs/technical/atbd_mod25.pdf
52. England, M., Jahn, A. & Polvani, L. Nonuniform contribution of internal variability to recent Arctic sea ice loss. *J. Clim.* **32**, 4039–4053 (2019).
53. Dörr, J. S., Bonan, D. B., Årthun, M., Svendsen, L. & Wills, R. C. Forced and internal components of observed Arctic sea-ice changes. *Cryosphere*, 17, 4133–4153 (2023); https://doi.org/10.5194/tc-17-4133-2023
54. Koenigk, T. & Brodeau, L. Ocean heat transport into the Arctic in the twentieth and twenty-first century in EC-Earth. *Clim. Dynam.* **42**, 3101–3120 (2014).
55. Serreze, M. C., Crawford, A. D., Stroeve, J. C., Barrett, A. P. & Woodgate, R. A. Variability, trends, and predictability of seasonal sea ice retreat and advance in the Chukchi Sea. *J. Geophys. Res. Oceans* **121**, 7308–7325 (2016).
56. Kodaira, T., Waseda, T., Nose, T. & Inoue, J. Record high Pacific Arctic seawater temperatures and delayed sea ice advance in response to episodic atmospheric blocking. *Sci. Rep.* **10**, 20830 (2020).
57. Steele, M., Zhang, J. & Ermold, W. Mechanisms of summertime upper Arctic Ocean warming and the effect on sea ice melt. *J. Geophys. Res. Oceans* **115**, C11004 (2010); https://doi.org/10.1029/2009JC005849
58. Maslanik, J. et al. A younger, thinner Arctic ice cover: increased potential for rapid, extensive sea-ice loss. *Geophys. Res. Lett.* **34**, L24501 (2007); https://doi.org/10.1029/2007GL032043
59. Ricker, R. et al. Satellite-observed drop of Arctic sea ice growth in winter 2015–2016. *Geophys. Res. Lett.* **44**, 3236–3245 (2017).
60. Polyakov, I. V. et al. Borealization of the Arctic Ocean in response to anomalous advection from sub-Arctic seas. *Front. Mar. Sci.* **7**, 491 (2020).
61. Shu, Q. et al. Arctic Ocean amplification in a warming climate in CMIP6 models. *Sci. Adv.* **8**, eabn9755 (2022).
62. Dörr, J., Årthun, M., Eldevik, T. & Sandø, A. B. Expanding influence of Atlantic and Pacific Ocean heat transport on winter sea-ice variability in a warming Arctic. *J. Geophys. Res. Oceans* **129**, e2023JC019900 (2024).
63. Meier, W. N., Fetterer, F., Windnagel, A. K. and Stewart, J. S. *NOAA/NSIDC Climate Data Record of Passive Microwave Sea Ice Concentration, Version 4* (NOAA, 2021); https://doi.org/10.7265/efmz-2t65

Methods

CESM simulations

HR and LR simulations were based on CESM1.3, for which the atmospheric component is the Community Atmosphere Model version 5 (CAM5) with the Spectral Element dynamical core, the ocean component is the Parallel Ocean Program version 2 (POP2), the sea-ice component is the Community Ice Code version 4 (CICE4) and the land component is the Community Land Model version 4 (CLM4). HR had a nominal horizontal resolution of 0.1° for the ocean and sea-ice components and 0.25° for the atmosphere and land components, whereas LR had a nominal horizontal resolution of 1° for all components. Both HR and LR produced a 500 yr pre-industrial control (PI-CNTL) climate simulation and a historical-and-future transient (HF-TNST) climate simulation from 1850–2100. PI-CNTL was forced by a perpetual climate forcing that corresponded to the 1850 conditions, whereas HF-TNST was branched from PI-CNTL at year 250 and forced by the observed climate forcing until 2005, after which the climate forcing followed a high-emissions scenario (that is, RCP8.5). For HR, two additional HF-TNST simulations were performed, branched from the 1850–2100 HF-TNST in 1920 with slightly different atmospheric initial conditions. Thus, an ensemble of three HR HF-TNST simulations is presented in this study. Similarly, five ensemble members of LR HF-TNST simulations were used in the present work.

Inferred calculation method for estimating OHT

Data from two mooring sites were used to obtain the observational OHT estimate[32]: A3 (66.3° N, 169° W) and A4 (65.6° N, 168.3° W) as shown in Fig. 1a. These two points were also utilized to compute CESM OHT using the inferred calculation method. To calculate OHT, the reference temperature (that is, freezing point) was −1.8 °C in CESM and −1.9 °C in the observational estimates. Away from the Alaska Coastal Current (ACC), velocity shows barotropic structures, while temperature shows a two-layer structure in the vertical in non-winter seasons. As shown by observations in previous work[31,32,64–66], the temperature from A3 can be used as a best approximation of the mean properties of non-ACC waters of the Bering Strait. Therefore, SST, combined with the temperature at 45 m (midpoint between 40 and 50 m) in HR and that at 25 m (midpoint between 20 and 30 m) in LR at A3 was used to capture the two-layer structure. The depth of 25 m was used in LR because the configured Bering Strait was shallower in LR than in HR. In addition, the depths at which meridional velocity (v) was used in CESM were 45 m in HR and 25 m in LR. They were the most consistent respective model depths with the one used in observational estimates (43 m). The stratification correction was $2 \times (\mathrm{SST}_{\mathrm{A3}} - T_{45\mathrm{m,A3}}) \times v_{45\mathrm{m,A3}}$ in HR and $2 \times (\mathrm{SST}_{\mathrm{A3}} - \mathrm{T}_{25\mathrm{m,A3}}) \times v_{25\mathrm{m,A3}}$ in LR. As v at 15 m can be regarded as the depth-averaged flow in the ACC region, the ACC correction for OHT across Bering Strait was calculated as $2 \times (T_{35\mathrm{m,A4}} + 1.8) \times (v_{15\mathrm{m,A4}} - v_{45\mathrm{m,A3}})$ in HR and $2 \times (T_{25\mathrm{m,A4}} + 1.8) \times (v_{15\mathrm{m,A4}} - v_{25\mathrm{m,A3}})$ in LR based on A4 data. Finally, the estimate for Bering Strait OHT was the sum of OHT at A3, the stratification correction and the ACC correction. The corresponding volume transport included estimates at A3 and the ACC correction.

A comparison between the model OHT computed using the inferred calculation method and that from the direct model output showed excellent agreement in HR, but in LR the model-derived OHT was substantially larger than that computed by the inferred calculation method (Extended Data Fig. 1). The disparity between the inferred calculation method-computed and model output OHT in LR implies that the temperature from A3 is insufficient to represent the mean properties of non-ACC waters of the Bering Strait, which was improved in HR.

Decomposition of OHT

The total OHT through the Bering Strait (~66° N) was directly output by the model. The mean-flow-induced OHT (MOHT) could be calculated with monthly mean meridional velocity ($\bar{v}$) and temperature ($\bar{T}$) as $\iint \bar{v}\bar{T}\mathrm{d}x\mathrm{d}z$, where d$x$ and dz are increments along the axes of longitude and depth, respectively. The eddy-induced OHT could be obtained through the difference between monthly OHT and MOHT, which was negligible at the Bering Strait (Extended Data Fig. 5); that is, OHT ≈ MOHT. Changes in OHT ($(\bar{v}\bar{T})_{t2} - (\bar{v}\bar{T})_{t1}$) can be further decomposed into the components associated with velocity change and temperature change as:

$$(\bar{v}\bar{T})_{t2} - (\bar{v}\bar{T})_{t1} = (\bar{v}_{t2} - \bar{v}_{t1})\,\bar{T}_{t1} + (\bar{T}_{t2} - \bar{T}_{t1})\,\bar{v}_{t1} + (\bar{v}_{t2} - \bar{v}_{t1})\,(\bar{T}_{t2} - \bar{T}_{t1}),$$

where $t1$ is the current period and $t2$ is the future period. The first and second terms on the right-hand side are contributions from the circulation change (that is, $T\Delta v$) and temperature change (that is, $v\Delta T$), respectively. The last term on the right-hand side is the nonlinear interaction of changes in circulation and temperature (that is, $\Delta v\Delta T$), which is small (Extended Data Fig. 5).

Bootstrap sampling

This method aims to minimize the impact of interannual variability on the seasonal cycle of OHT. With the assumption that the OHT seasonal cycle did not change appreciably over the period 1950–2019, we randomly drew 13 years from 1950–2019 to construct a seasonal cycle of OHT and repeated this process 1,000 times.

OHT in CMIP5

Given the minimal impact of eddies on Bering Strait OHT (Extended Data Fig. 5), the total OHT in CMIP5 models can be estimated by integrating the product $\bar{v}$ and $\bar{T}$ in the zonal and vertical directions, represented as $\iint \bar{v}\bar{T}\mathrm{d}x\mathrm{d}z$.

Data availability

The CMIP5 data used in this study can be downloaded from https://esgf-node.llnl.gov/search/cmip5/. The CESM data used in this work are available from https://ihesp.github.io/archive/products/ihesp-products/data-release/DataRelease_Phase2.html. The MODIS data can be download from http://apdrc.soest.hawaii.edu/data/data.php. The mooring data can be downloaded from https://psc.apl.washington.edu/HLD/Bstrait/Data/BeringStraitMooringDataArchive.html.

Code availability

The CESM codes are available via GitHub at https://github.com/ihesp/CESM_SW (ref. 67).

References

64. Woodgate, R. A., Aagaard, K. & Weingartner, T. J. Interannual changes in the Bering Strait fluxes of volume, heat and freshwater between 1991 and 2004. *Geophys. Res. Lett.* **33**, L15609 (2006); https://doi.org/10.1029/2006GL026931
65. Woodgate, R. A., Weingartner, T. J. & Lindsay, R. Observed increases in Bering Strait oceanic fluxes from the Pacific to the Arctic from 2001 to 2011 and their impacts on the Arctic Ocean water column. *Geophys. Res. Lett.* **39**, L24603 (2012); https://doi.org/10.1029/2012GL054092
66. Woodgate, R. A., Stafford, K. M. & Prahl, F. G. A synthesis of year-round interdisciplinary mooring measurements in the Bering Strait (1990–2014) and the RUSALCA years (2004–2011). *Oceanography* **28**, 46–67 (2015).
67. ihesp/CESM_SW: Community Earth System Model (CESM1.3.1) on the Sunway TaihuLight supercomputer. *Zenodo* https://doi.org/10.5281/zenodo.10888306 (2024).

Acknowledgements

The high-resolution CESM simulations were initiated by the International Laboratory for High-Resolution Earth System

Prediction—a collaboration between the Qingdao Pilot National Laboratory for Marine Science and Technology, Texas A&M University and the US National Science Foundation (NSF) National Center for Atmospheric Research (NCAR). A major portion of the high-resolution CESM simulations were completed on Frontera at the Texas Advanced Computing Center (TACC) of the University of Texas at Austin, TX, United States, under project number ATM20005. We thank J. Edwards for his assistance in porting and optimizing the CESM code on Frontera at TACC. P.C., G.D., S.G.Y., F.C., G.X. and Q.Z. are supported by the National Academies of Science and Engineering Gulf Research Program grant number 2000013283 and the US NSF grant number AGS-2231237. S.G.Y., P.C. and Q.Z. are supported by the Department of Commerce grant number NA20OAR4310408. M.S. is supported by NASA grant number 80NSSC20K0768, NSF grant number OPP-1751363 and ONR grant number N00014-21-1-2868. W.W. and Y.L. were supported by the Regional and Global Model Analysis (RGMA) component of the Earth and Environmental System Modeling programme of the US Department of Energy's Office of Science, as a contribution to the HiLAT-RASM project. Y.L. was also supported by the Center for Nonlinear Studies at Los Alamos National Laboratory. N.R. is supported by the US Department of Energy, Office of Science, Office of Biological & Environmental Research RGMA component of the Earth and Environmental System Modeling Program under award number DE-SC0022070. NSF NCAR is a major facility sponsored by the US NSF under cooperative agreement number 1852977.

Author contributions

P.C. conceptualized the study. P.C., G.X., M.C.R. and X.L. conducted the investigation. Q.Z., N.R., F.C. and S.G.Y. ran the simulations. G.X., M.C.R. and X.L. performed the analysis. G.X. visualized the data. P.C. and G.D. acquired funding. G.X. and M.C.R. wrote the original draft, P.C., G.D., M.S., W.W., S.G.Y., Y.L. and G.X. reviewed and edited the manuscript.

Competing interests

The authors declare no competing interests.

Additional information

Extended data is available for this paper at https://doi.org/10.1038/s41558-024-02008-z.

Supplementary information The online version contains supplementary material available at https://doi.org/10.1038/s41558-024-02008-z.

Correspondence and requests for materials should be addressed to Ping Chang.

Peer review information *Nature Climate Change* thanks David Docquier and the other, anonymous, reviewer(s) for their contribution to the peer review of this work.

https://doi.org/10.1038/s41558-024-02008-z

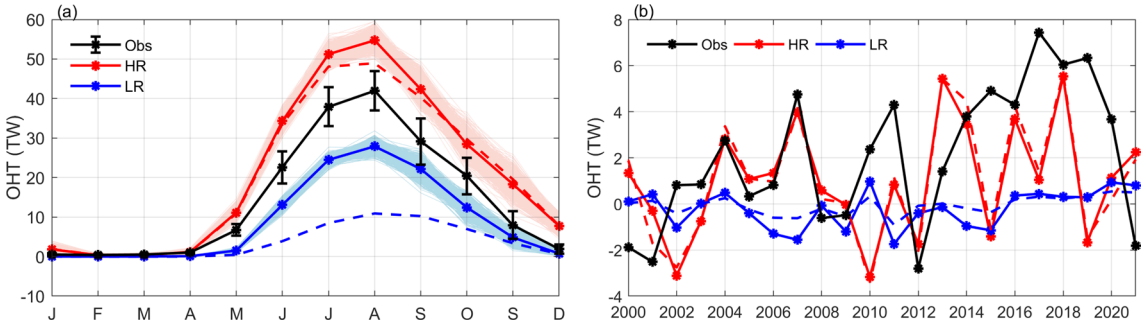

Extended Data Fig. 1 | Inferred calculation method computed OHT. (**a**-**b**) Similar to Fig. 1e & g, respectively, but includes both inferred calculation method-computed (dashed) and model-derived (solid) OHT in HR (red) and LR (blue). Error bars in (**a**) are the 95% limit of a 1-side Student's t-test with the degree of freedom as 13.

https://doi.org/10.1038/s41558-024-02008-z

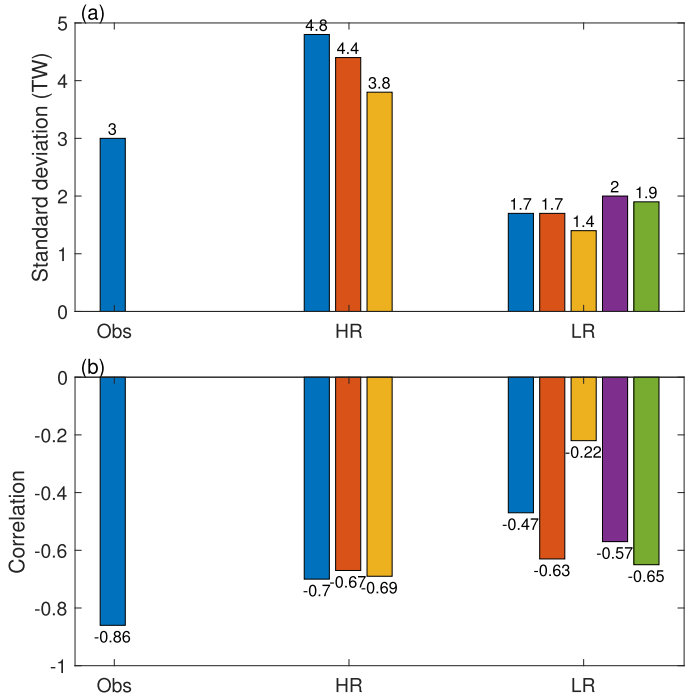

Extended Data Fig. 2 | Standard deviation of OHT and correlation coefficient between detrended sea ice area and OHT. (**a**) The standard deviation of OHT from 2000 to 2021 in observations, HR, and LR. (**b**) The correlation coefficient between detrended sea ice area and OHT anomaly from 2000 to 2021 in observations, HR, and LR. Different colors in each group represent different ensemble members. The correlation coefficients are significant at 95% confidence level but not from LR ensemble #3 (−0.22). Different colors in each group represent different ensemble members.

https://doi.org/10.1038/s41558-024-02008-z

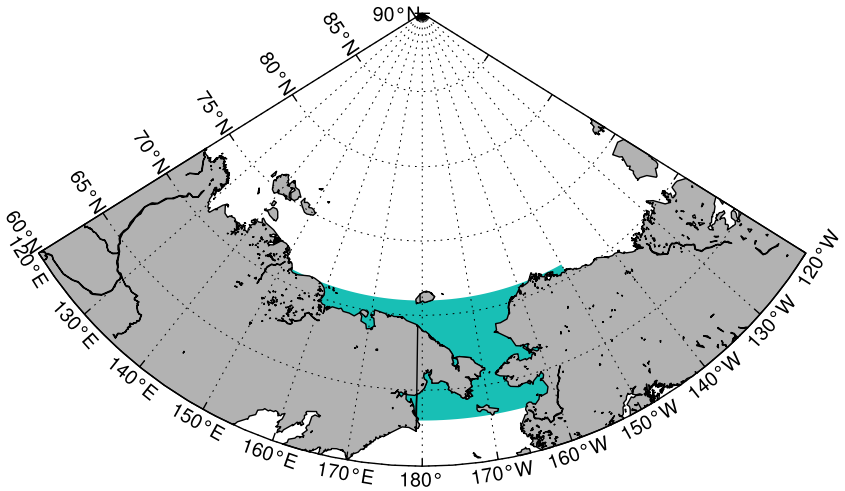

Extended Data Fig. 3 | Definition of the region near the Bering Strait. Area with green shading is used to construct sea ice timeseries near the Bering Strait in Fig. 1h.

https://doi.org/10.1038/s41558-024-02008-z

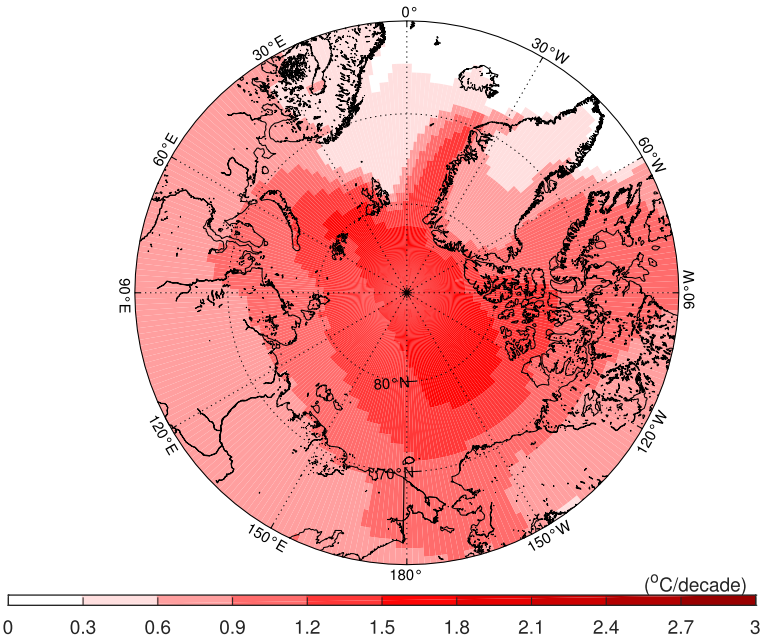

Extended Data Fig. 4 | Projected Arctic warming. The rate of surface air temperature changes in LR over the period 2006–2100.

https://doi.org/10.1038/s41558-024-02008-z

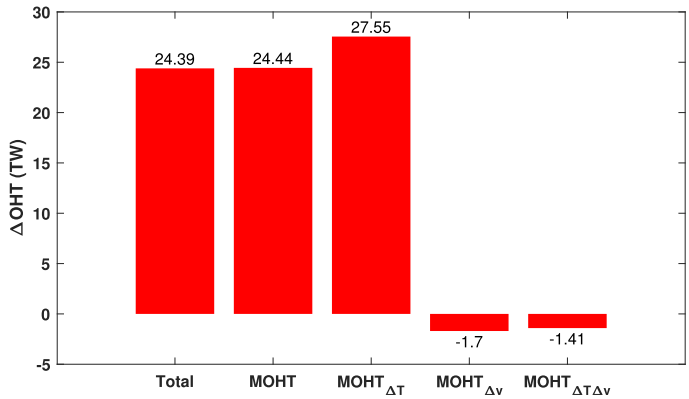

Extended Data Fig. 5 | Decomposition of changes in the Bering Strait OHT in HR. The change is defined as the difference between the mean over 2081–2100 and that over 2006–2025. MOHT: monthly-mean OHT changes computed using monthly-mean temperature and velocity output; MOHTΔT: change in MOHT due to temperature change ΔT; MOHTΔv: change in MOHT due to velocity change Δv; MOHTΔTΔv: change in MOHT due to the nonlinear product of temperature and velocity change ΔTΔv.

https://doi.org/10.1038/s41558-024-02008-z

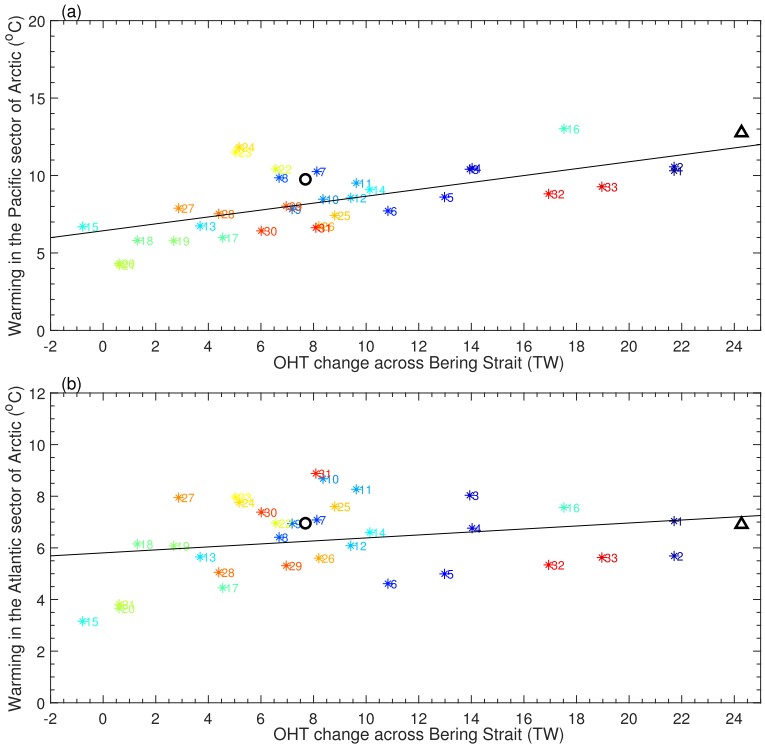

Extended Data Fig. 6 | Scatterplot of changes in annual-mean Bering Strait OHT and Arctic surface air temperature over the Pacific and Atlantic sectors. (**a**) Arctic surface air temperature over the Pacific sector and (**b**) the Atlantic sector of the Arctic from HR (triangle), LR (circle), and CMIP5 models (stars). Changes are defined as the difference between the mean over 2081–2100 and that over 2006–2015. The linear regression in (**a**) has a slope of 0.22 °C TW^{-1} and is significant at a 95% confidence level, while the linear regression in (**b**) has a slope of 0.06 °C TW^{-1} and is not statistically significant at a 95% confidence level.

https://doi.org/10.1038/s41558-024-02008-z

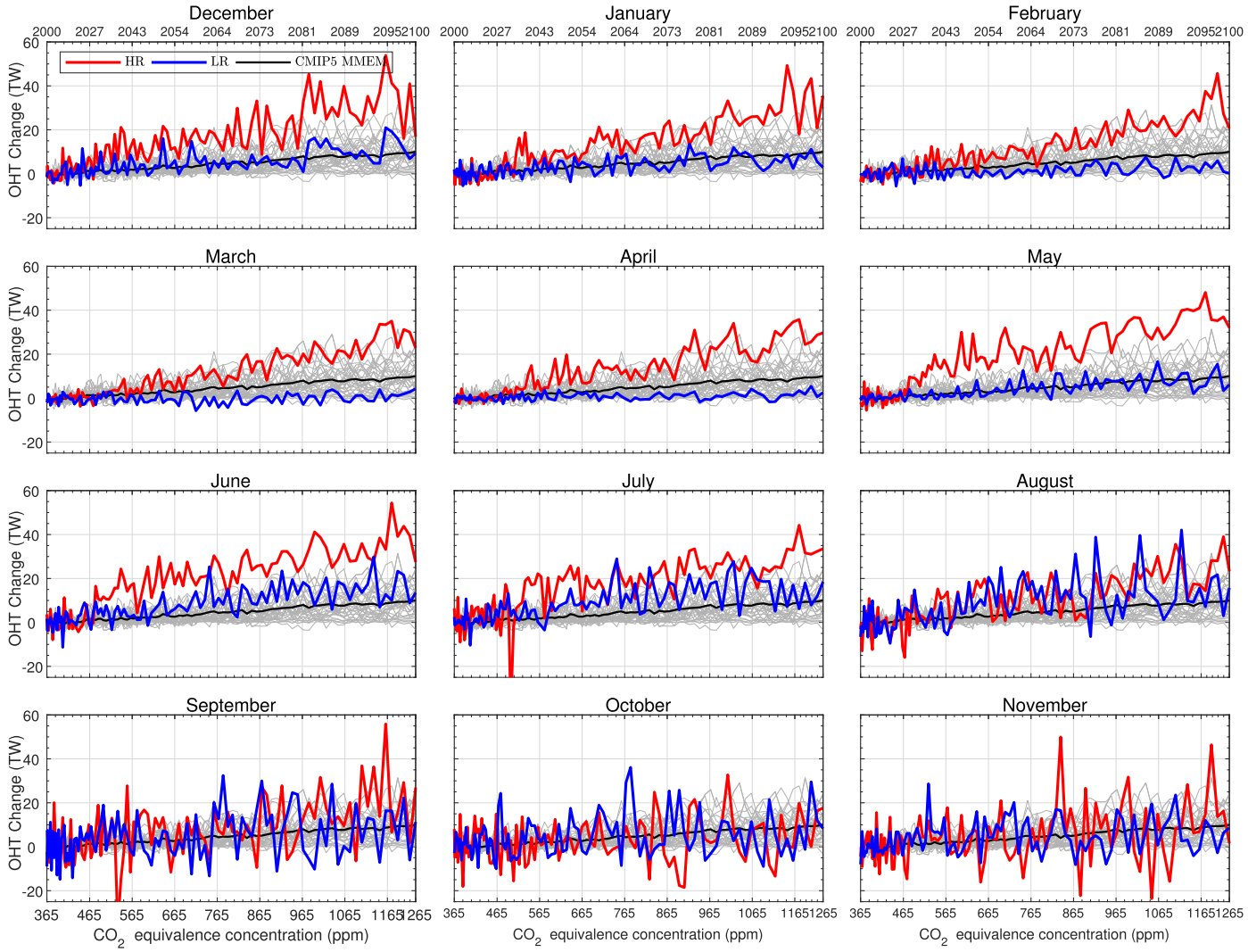

Extended Data Fig. 7 | Monthly Bering Strait OHT anomaly relative to the mean over 2006–2015. Results are from HR (red), LR (blue), and CMIP5 models with RCP8.5 forcing (gray) as a function of CO_2 concentration increase (bottom x-axis) and time (top x-axis). Black for the CMIP5 multi-model ensemble mean.

https://doi.org/10.1038/s41558-024-02008-z

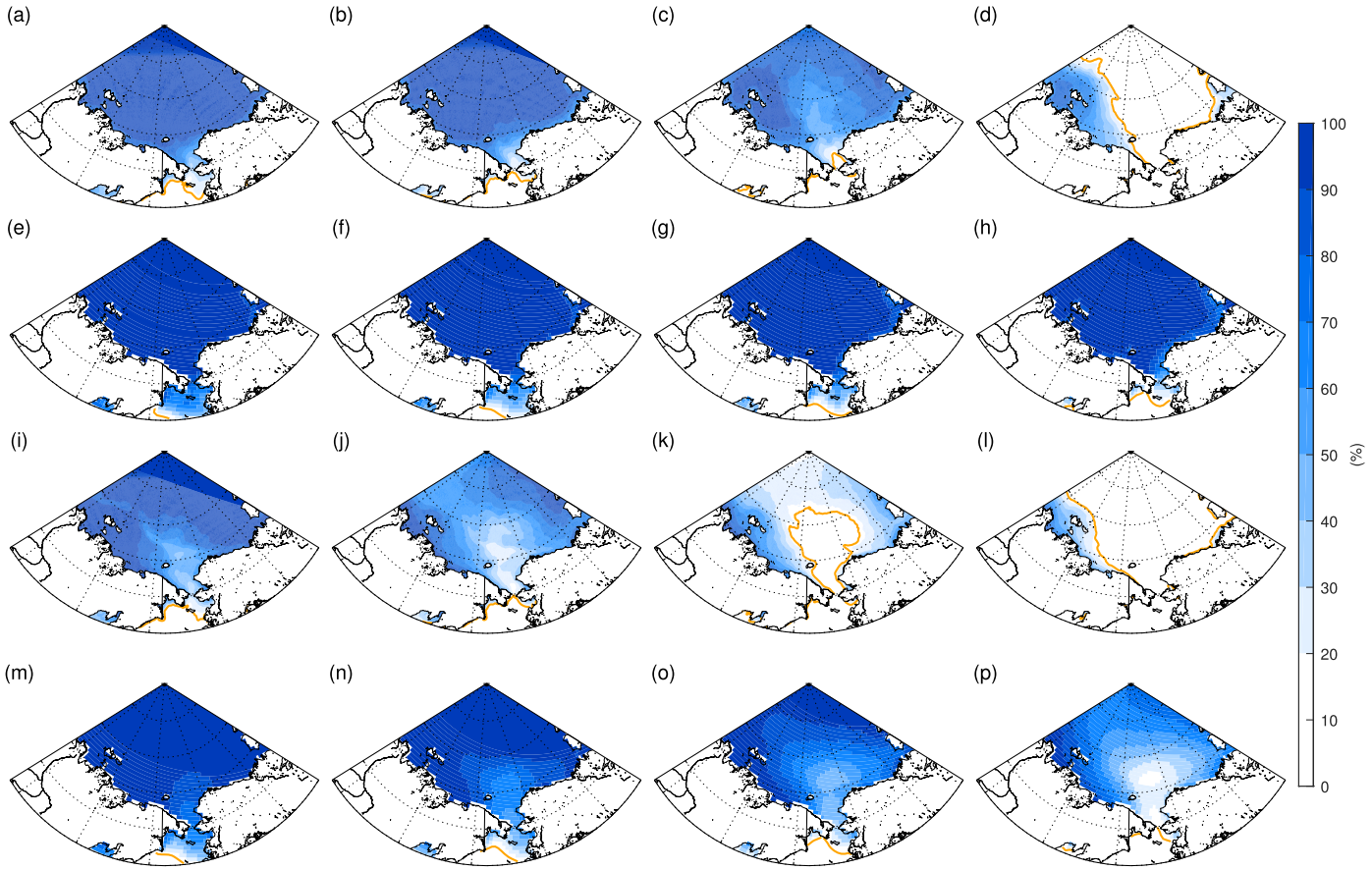

Extended Data Fig. 8 | Sea ice concentration during different periods. (**a**-**d**) Sea ice concentration in MAM in HR. (**e**-**h**) Similar to **a**-**d**, but in LR. (**i**-**l**) Sea ice concentration in DJF in HR. (**m**-**p**) Similar to **i**-**l**, but in LR. Orange contour is sea ice edge defined as 15% sea ice concentration.

https://doi.org/10.1038/s41558-024-02008-z

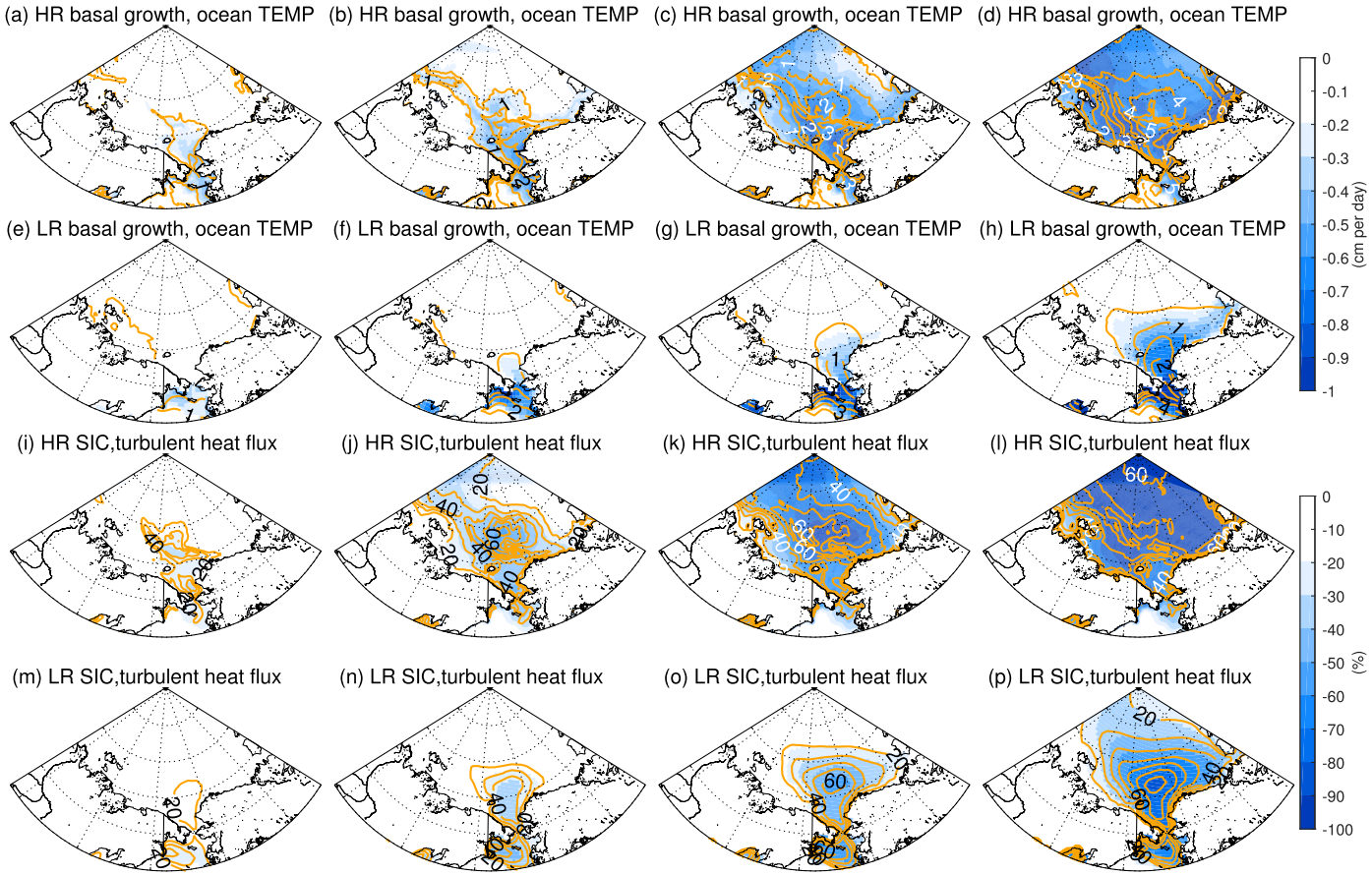

Extended Data Fig. 9 | Future changes in basal sea ice growth, upper-50-m-ocean temperature, sea ice concentration, and surface heat fluxes. (**a**-**d**) Changes in basal growth of sea ice (ocean temperature in the upper 50 m) during boreal winter (DJF) in HR depicted by color shades (contours). (**e**-**h**) Same as **a**-**d** but for LR. (**i**-**l**) Changes in sea ice concentration (turbulent heat flux) during boreal winter (DJF) in HR depicted by color shades (contours). (**m**-**p**) Same as **i**-**l** but for LR. The first to fourth column represents changes averaged over 2030–2039, 2050–2059, 2070–2079, and 2090–2099 relative to the mean over 2006–2015, respectively. Contour interval in **a**-**h** is 0.5 °C and in **i**-**p** is 10 Wm^{-2}.

https://doi.org/10.1038/s41558-024-02008-z

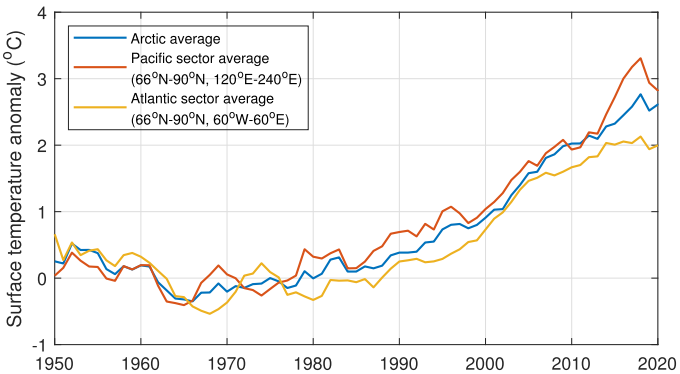

Extended Data Fig. 10 | Observed surface air temperature anomalies relative to the 1950–1980 mean. GISTEMPv4 annual-mean surface air temperature anomalies from 1950 to 2020, relative to the 1950–1980 mean, averaged over the Arctic region (blue), Pacific sector of the Arctic (red), and Atlantic sector of the Arctic (orange). The Pacific sector covers the area from 66°N to 90°N and from 120°E to 240°E. The Atlantic sector covers the area from 66°N to 90°N and from 60°W to 60°E.